

Trace Analysis and Reaction Monitoring by Nanophotonic Ionization Mass Spectrometry from Elevated Bowtie and Silicon Nanopost Arrays

Sylwia A. Stopka,* Xavier A. Holmes, Andrew R. Korte, Laine R. Compton, Scott T. Retterer, and Akos Vertes*

Silicon nanopost arrays (NAPA) are used in trace analysis by mass spectrometry (MS) because they enable highly efficient ion production from small molecules and thin tissue sections by UV laser desorption ionization (LDI). Such nanophotonic ionization of adsorbates relies on localized interactions between a nanostructured substrate and laser radiation. In LDI from NAPA, only the component of the oscillating electric field vector that is parallel with the posts couples the laser energy into the nanostructure. Enhancements in control over adsorbate ionization and fragmentation are expected if the surface-parallel component can also interact with the nanostructure. Here, an alternative nanophotonic ionization platform is introduced for LDI-MS, the elevated bowtie (EBT) array by adding triangular chromium features on top of silicon post pairs to form bowties. Compared to NAPA, the threshold fluence for ionization from EBT is lower, and at low laser fluences the ionization efficiency is increased by a factor of ≈ 17 . The EBT platform with optimized apex angle exhibits a higher survival yield for molecular ions produced from biomolecules and xenobiotics and allows more control over fragmentation by adjusting the fluence. These unique nanophotonic ionization attributes are utilized for trace analysis and reaction monitoring in complex biological samples.

1. Introduction

When the dimensions of a nanostructure are commensurate with the wavelength of the electromagnetic radiation, surface adsorbates can undergo efficient nanophotonic ionization based on near-field enhancement of the electric field.^[1] Several nanophotonic applications utilize the dynamic lightning


rod effect for near-field enhancement and localization at the apex by implementing nanotips to overcome the diffraction limit, e.g., scanning near-field optical microscopy (SNOM) and nanoscale chemical analysis by tip-enhanced Raman scattering (TERS).^[2] For example, using an antenna-based scanning near-field optical microscope for molecular fluorescence and modeling revealed a near-field enhancement factor of 40 which corresponded to a $\approx 10^3$ fold-increase in near-field laser intensity at the apex of the probe.^[3] The bowtie configuration based on triangular geometry is one of the most studied nanostructures due to the near-field enhancement within the gap region of two metal nanotriangles in close proximity. For example, the use of gold bowties yielded significant enhancement of single-molecule fluorescence.^[4] Furthermore, through surface plasmon resonance an electric-field enhancement of $\approx 10^5$ was observed within a 2 nm gap between two nanoparticles; however, this enhancement weakened as the gap region increased.^[5] Applications

of the bowtie optical antennas include integrated nanophotonic devices, data storage, and super-resolution microscopy.^[6]

Mass spectrometry (MS) is a powerful analytical tool capable of the simultaneous detection and spatial mapping of various biomolecules, e.g., metabolites, lipids, and peptides from biological mixtures and tissue sections.^[7] However, the most commonly used soft-ionization technique, matrix-assisted laser desorption ionization (MALDI) MS results in ion suppression and spectral interferences arising from the organic matrix. It also suffers from poor shot-to-shot reproducibility, making quantitative measurements challenging.^[8] To overcome these limitations, nanomaterials have been introduced as an alternative to organic matrixes for laser desorption ionization (LDI). In general, nanomaterials possess unique electrical, optical, and thermal properties, resulting in a variety of bioanalytical applications from MS-based techniques to lab-on-a-chip microfluidic devices.^[9] These nanostructured substrates, acting as the energy-absorbing material for LDI-MS, have significant advantages, e.g., minimal sample preparation, reduced chemical interference, detection of small biomolecules, and high-throughput capabilities.^[10]

Dr. S. A. Stopka, X. A. Holmes, Dr. A. R. Korte, L. R. Compton, Prof. A. Vertes
Department of Chemistry
The George Washington University
Washington, DC 20052, USA
E-mail: stopka@gwmail.gwu.edu; vertes@gwu.edu

Dr. S. T. Retterer
Center for Nanophase Materials Science and Biosciences Division
Oak Ridge National Laboratory
Oak Ridge, TN 37831, USA

 The ORCID identification number(s) for the author(s) of this article can be found under <https://doi.org/10.1002/adfm.201801730>.

DOI: 10.1002/adfm.201801730

Over the past decade an assortment of matrix-free LDI-MS techniques (e.g., surface-assisted LDI^[11]) has been introduced with variations in the substrate materials and nanostructures for a wide range of applications.^[12] For example, utilizing carbon as the substrate, nanodiamonds,^[13] graphene nanoflakes,^[14] and oxidized carbon nanotubes^[15] have been used for protein, lipid, and amino acid detection by MS-approaches, respectively. Other popular matrix-free LDI-MS substrates include titanium dioxide nanocrystals,^[16] nanoflowers,^[17] patterned nanostructured gold thin film,^[18] nanostructured indium tin oxide coated slides,^[19] and diamond nanowires.^[20] Due to their excellent thermal and electrical properties, silicon nanomaterials are very common. Applications include desorption ionization on silicon (DIOS),^[21] silicon nanowires,^[22] nanostructure initiator mass spectrometry (NIMS),^[23] and silicon nanopost arrays (NAPA).^[24] Additionally, surface modifications of these nanomaterials for selective biomolecule capture has been reported, e.g., surfaces of DIOS modified by avidin–biotin binding^[25] and antibody immobilization,^[26] and gold manganese oxide hybrid nanoflowers functionalized with aptamers.^[17] Plasmon resonance has been integrated with LDI-MS using gold nanoshells for the analysis of amino acids directly from serum samples.^[27] Highly ordered monolithic structures such as NAPA can be fabricated by lithography-based approaches, which result in exquisite control of the nanostructure dimensions, down to the nanometer scale. Moreover, due to the nanoscale patterning of the posts, this allows for homogenous analyte deposition.

In previous work, we demonstrated the utility of LDI from NAPA for the analysis of volume-limited samples, e.g., a single yeast cell, small molecule quantitation from human serum, and MS imaging of biological tissues.^[24b,28] Herein we introduce a new matrix-free LDI-MS nanostructured substrate consisting of an array of elevated bowtie antennas (EBT) for the ionization and trace analysis of biomolecules. We explore ion production as a function of tip sharpness in three EBT configurations with varied apex angles. To examine the degree of near-field enhancement, finite-difference time-domain (FDTD) modeling is employed. By monitoring proteolytic digestion of small peptides as a function of time, we demonstrate that the ion yields reflect the quantity of surface adsorbates. Trace analysis is demonstrated in complex biological samples, such as cell extracts and tissue sections.

2. Nanophotonic Ion Production

To systematically compare ion production from NAPA and EBT arrays, a variety of nanostructures were fabricated. **Figure 1a** shows the dimensions of a single EBT with an antenna length (L) of, e.g., 240 nm composed of two rounded equilateral triangles, and a 40 nm gap (G) between them. The post height

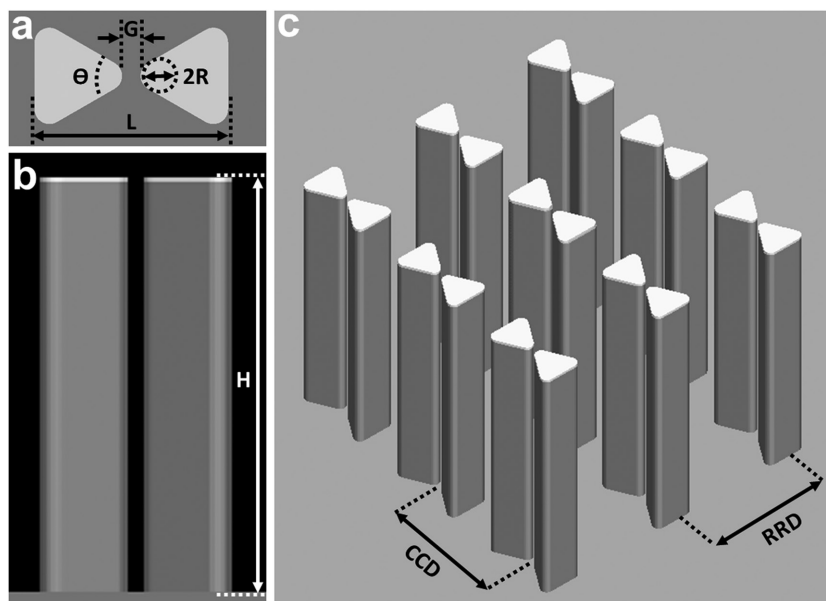


Figure 1. Schematic of elevated bowtie array. a) Top view shows definition of antenna length (L), gap size (G), apex angle (Θ), and radius of curvature (R). b) Side view shows post height (H) that determines elevation of bowties. c) 3D perspective of a bowtie array segment indicating center-to-center distance (CCD) and row-to-row distance (RRD) definitions.

(H) was kept constant at $H = 1200$ nm for all structures (see **Figure 1b**). To compare results from the EBT and NAPA structures, the center-to-center distance (CCD) of the bowties was made equal to the periodicity, P , of NAPA, i.e., $CCD = P = 337$ nm. The row-to-row distance (RRD) for EBT arrays was set to 254, 315, and 438 nm, for the $\Theta = 30^\circ$, 60° , and 100° apex angles, respectively (**Figure 1c**). To investigate if the presence of small gaps in the bowties played a role in ion generation, an isolated half-bowtie configuration was also fabricated by increasing the gap size to $G = 237$ nm, resulting in the same post-to-post distance as the NAPA periodicity, i.e., $P = 337$ nm. The number of bowties in a $500 \times 500 \mu\text{m}^2$ chip was calculated as $1484 \times 1969 = 2\,920\,629$, $1484 \times 1587 = 2\,355\,047$, and $1484 \times 1142 = 1\,693\,698$ for the 30° , 60° , and 100° EBTs, respectively.

The combined efficiency of desorption and ionization from the nanophotonic EBT substrates was explored as a function of laser fluence for verapamil, a small molecule often used for the characterization of ion production. Initial experiments were performed to compare the abundance of ions produced by LDI from NAPA, isolated EBT with a 60° apex angle, and EBT structures with a 60° apex angle (see the corresponding scanning electron microscope (SEM) images in **Figure 2b**) as a function of laser fluence in the 4–20 mJ cm^{-2} range. The combined intensities of the intact quasimolecular ion and the fragment ions produced by in-source decomposition for 50 pmol of verapamil were plotted as a function of laser fluence can be seen in **Figure 2a** (corresponding mass spectra are shown in **Figure S1** in the Supporting Information). As observed with other matrix-free LDI platforms, the precursor peak at m/z 455.2898 and the fragments at m/z 303.2062 and 165.0905 were predominant with no interfering background.^[29] The fluence threshold for the production of protonated molecules from the 60° EBT arrays was 4 mJ cm^{-2} ($S/N = 6924$) compared to 8 mJ cm^{-2} for

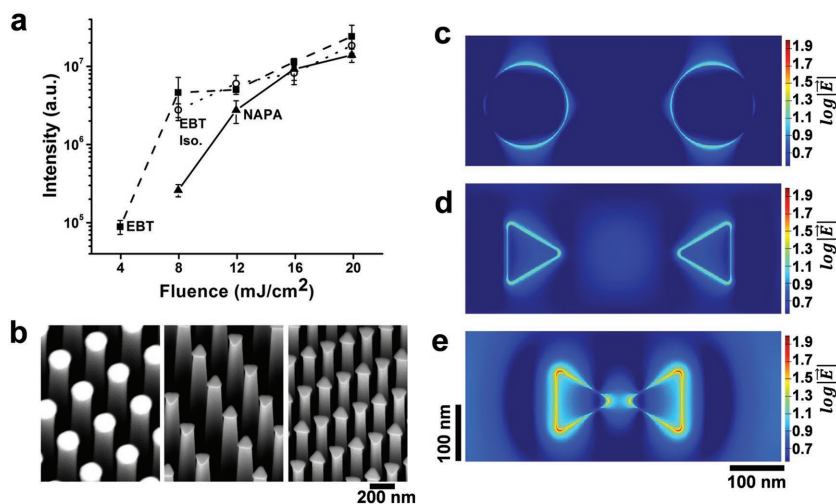


Figure 2. Comparison of ion production and electric field enhancement on NAPA, isolated 60° EBT, and 60° EBT nanostructures. a) Combined intensities of precursor and fragment ions for 50 pmol of verapamil produced by LDI from NAPA, isolated 60° EBT, and 60° EBT as a function of laser fluence ranging from 4 to 20 mJ cm⁻². b) Scanning electron microscope images of (left) NAPA, (middle) isolated EBT, and (right) $\Theta = 60^\circ$ EBT. Contour plots of electric field amplitudes in top view displayed on logarithmic jet color scale for c) NAPA, d) isolated 60° EBT, and e) 60° EBT for 337 nm laser beam polarized along *x*-axis. Laser light was injected from top of nanostructure at a 32° angle from surface normal and in plane with the bowtie axis. Electric field amplitudes were calculated by FDTD.

the NAPA ($S/N = 7834$) and isolated EBT ($S/N = 6938$) structures. At 8 mJ cm⁻², the EBT exhibited ≈ 17.8 times higher ion intensity compared to the NAPA structures.

As for nanostructured substrates the internal energy of an ion and its fragmentation are dependent on the laser fluence, low fluence spectra can be used for molecular weight determination, whereas high fluence spectra provide structural information. For NAPA, EBT and isolated EBT, the degree of in-source fragmentation was varied by adjusting the laser fluence. For example, at a low 8 mJ cm⁻² fluence only the quasimolecular verapamil ion was detected from NAPA, whereas the isolated EBT and EBT exhibited in-source fragmentation of $17.4 \pm 0.4\%$ and $22.1 \pm 2.3\%$, respectively. Two likely sources of the difference in fragmentation between the NAPA and isolated EBT structures are the presence of sharp corners on the chromium triangles in the latter, and the difference between the cross-sectional areas of the two structures. An additional small increase in fragmentation is observed when the isolated EBT are transformed into EBTs with significantly smaller gaps. These observations point to the influence of elevated field strengths in these structures. At a laser fluence of 20 mJ cm⁻², the NAPA and isolated EBT systems exhibited similar degrees of in-source fragmentation, i.e., $45.4 \pm 0.6\%$ and $46.0 \pm 2.0\%$, respectively, whereas the EBT structure showed slightly higher fragmentation at $51 \pm 2.7\%$. This minor increase can also be explained by the presence of higher electric field strengths in the gap region of these structures. To assess the extent of damage produced on these nanostructures by the laser pulses, SEM images were taken of the 60° EBTs at several laser fluences (See Figure S2 in the Supporting Information). No post damage was observed at low laser fluences ranging from 0 to 4 mJ cm⁻². The post tips started to show some degree of melting around 8 mJ cm⁻² and

extensive melting at 24 mJ cm⁻². This surface melting at higher laser fluences observation is consistent with other matrix-free LDI-MS methods.^[30] At these elevated fluences, the chromium EBTs on the top of the posts were clearly obliterated, and the structures were working similarly to the NAPA structures as shown in Figure 2a where the ionization efficiency of EBT approaches that of NAPA at 12 mJ cm⁻² and above.

3. Mapping Electric-Field Distributions for Near-Field Enhancements

To identify the electric field distributions induced by the interactions between these structures and the laser radiation, we performed FDTD calculations. We compare the amplitudes of the electric field distributions for the three different structures in contour plots for the *x*-*z* side views and *x*-*y* top views (see Figure 2c–e). Past comparisons of the electric field distributions induced around circular and triangular discs indicated significant field enhancement around the corners of the latter structures.^[31] This is corroborated by our calculations that indicate slightly higher near-field effects at the corners of the isolated EBT compared to the NAPA design (compare the field distributions in Figure 2c,d). Additionally, in the EBT configuration strong electric field enhancement is observed in the gap region (see Figure 2e) due to current oscillations along the bowtie axis.

4. Bowtie Apex-Angle Dependence on Ion Production

To evaluate the effect of bowtie antenna sharpness on ion production, EBTs with apex angles of $\Theta = 30^\circ$, 60° , and 100° were produced, verapamil samples were deposited, and the structures were irradiated by laser pulses. The combined ion intensities of the quasimolecular and fragment ions as a function of the laser fluence are shown in Figure 3a (corresponding mass spectra are shown in Figure S3 in the Supporting Information). At a low laser fluence of 4 mJ cm⁻² only the EBT with apex angles of $\Theta = 30^\circ$ and 60° produced detectable quantities of verapamil ions. At 8 mJ cm⁻², ions were detected from EBTs of all three apex angles; however, the 30° structure produced the highest ion intensity with 2.3- and 26.1-fold improvements over the EBTs with 60° and 100° apex angles, respectively. As the laser fluence was increased, the combined intensity of verapamil ions grew for all apex angles, and at all fluences the 30° EBT was superior to the 60° EBT, and the 100° EBT substrate was the least efficient. All geometries exhibited higher ion yields as the laser fluence increased. For example, for the 30° EBT configuration ion yield improvements of a factor of ≈ 2.0 and ≈ 3.0 were observed, when the fluence increased from 8 to 12 mJ cm⁻²,

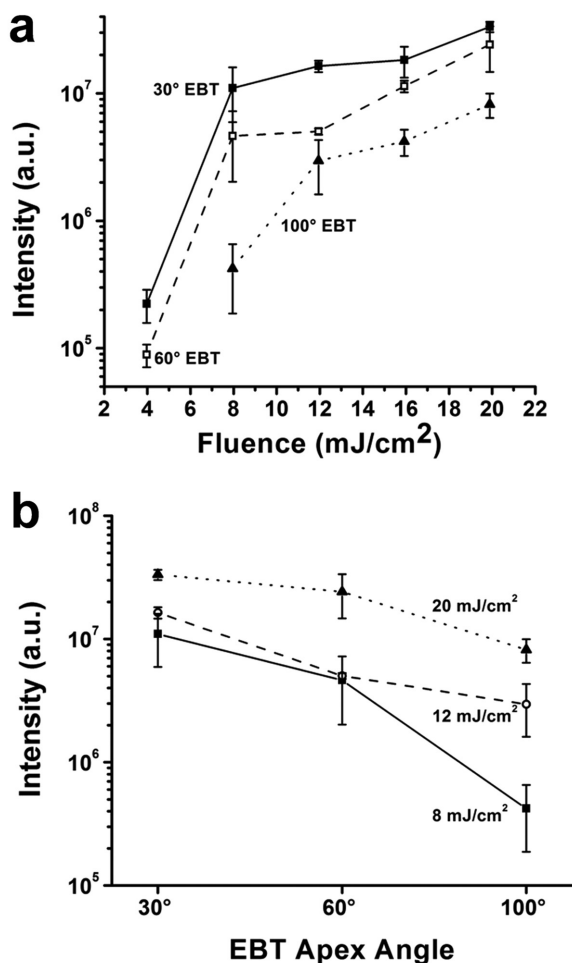


Figure 3. Fluence and apex angle dependence of verapamil ion intensities produced by LDI from EBT nanostructures. a) Ion intensities are highest for 30° EBT, followed by 60° EBT and 100° EBT at all fluence values. b) Ion intensities decline as the apex angle increases, with lowest fluence, 8 mJ cm⁻², showing the steepest drop. Accentuated differences are observed for 100° EBT.

and from 8 to 20 mJ cm⁻², respectively. Similar trends were observed for the 60° and 100° EBT geometries. However, higher laser fluences resulted in increased in-source fragmentation. For the geometry with the highest ion yield, the 30° EBT, the degree of in-source fragmentation for 8, 12, and 20 mJ cm⁻², was 29.0 ± 7.9%, 36.1 ± 0.4%, and 51.9 ± 1.1%, respectively.

As the apex angles of the bowties was varied from $\Theta = 30^\circ$ to 60°, and 100°, the corresponding radius of curvature, R , measured in the SEM images increased from $2R = 16 \pm 1$, to 32 ± 1 , and 41 ± 1 nm, respectively, and the ion yields dropped at all laser fluences (see Figure 3b). To explore the near-field enhancement of the electric field around the EBTs of varied apex angles, FDTD simulations were performed (see Figure 4). The results indicate that the surface orthogonal, p , and surface parallel, s , components of the oscillating electric field vector, E_p and E_s , respectively, induce corresponding current oscillations in the EBTs. The electric field amplitude distributions indicate

standing waves in the posts with an approximate wavelength of ≈ 255 nm created by the E_p oscillations showing deviations in wavelength at the top due to the presence of the chromium bowties and somewhat longer wavelength at the bottom due to the silicon base (see Figure 4b). The E_s component, parallel with the bowtie axis, couples strongly with the chromium structure, and produces electric field distributions familiar from conventional bowtie systems. Figure 4c presents the top view, zoomed to the gap region, for the electric field distributions. At the level of the chromium layer (an elevation of 1208 nm), the 30° EBT, 60° EBT, and 100° EBT exhibited relative field enhancements of 52, 47, and 36, respectively. It is interesting to compare the modest increase in field enhancement for the sharper structures with the significant rise in ion yield. As the maximum of the field enhancement grew by a factor of 1.4 between the 100° EBT and 30° EBT, the corresponding ion yield increased by a factor of 5.5 at 12 mJ cm⁻² fluence.

5. Structural Elucidation by In-Source Fragmentation

Ion fragmentation is often utilized for the determination of molecular structure. Fragmentation can be facilitated by raising the internal energy of the ions. As in MALDI experiments this can only be done to a limited degree by increasing the laser fluence, higher ion internal energies are achieved by selecting a different matrix that affords more in-source fragmentation. This approach can be applied for, e.g., structural studies of mid-sized peptides (>5000 Da).^[32] In nanophotonic ion sources, e.g., NAPA and its precursor, laser-induced silicon microcolumn arrays or LISMA, increasing the laser fluence directly leads to more extensive fragmentation.^[33] To explore the utility of this phenomenon for structural characterization, a synthetic peptide Pro₁₄-Arg (P₁₄R) was subjected to LDI from NAPA and EBT substrates at varying laser fluences (Figure 5). At the fluence threshold, ≈ 8 mJ cm⁻² for NAPA and ≈ 4 mJ cm⁻² for EBT, only the quasi-molecular ion, $[M+K]^+$ at m/z 1571.8072, is detected without fragmentation. As the fluence is increased, fragmentation is observed for both nanostructures, but the EBT provides more extensive fragmentation and consequently more extended sequence coverage. For EBT at ≈ 8 mJ cm⁻², both the low energy γ -series (γ_8 - γ_{14}) and the high energy a -series (a_7 - a_{13}) fragments are observed. At a laser fluence of ≈ 20 mJ cm⁻², structure-specific fragmentation is observed from both substrates, with the γ -series dominant in the spectra from NAPA, whereas the a -series is more abundant for the EBT substrate. Further increasing the laser fluence to ≈ 40 mJ cm⁻², resulted in more extended presence of high-energy a -series ions for NAPA, yielding spectra similar to those from EBT at ≈ 8 mJ cm⁻². This indicates that similar internal energies can be achieved by the latter at much lower fluences. At the highest studied laser fluence of ≈ 200 mJ cm⁻², the EBT produced an extended series of exclusively a -series ions, whereas LDI from NAPA resulted in a single structure-specific ion, a_9 . Overall, the EBT produced informative fragmentation in the fluence range between ≈ 8 and ≈ 200 mJ cm⁻², whereas the utility of NAPA structures was limited to the 20–40 mJ cm⁻² range. This finer control over ion

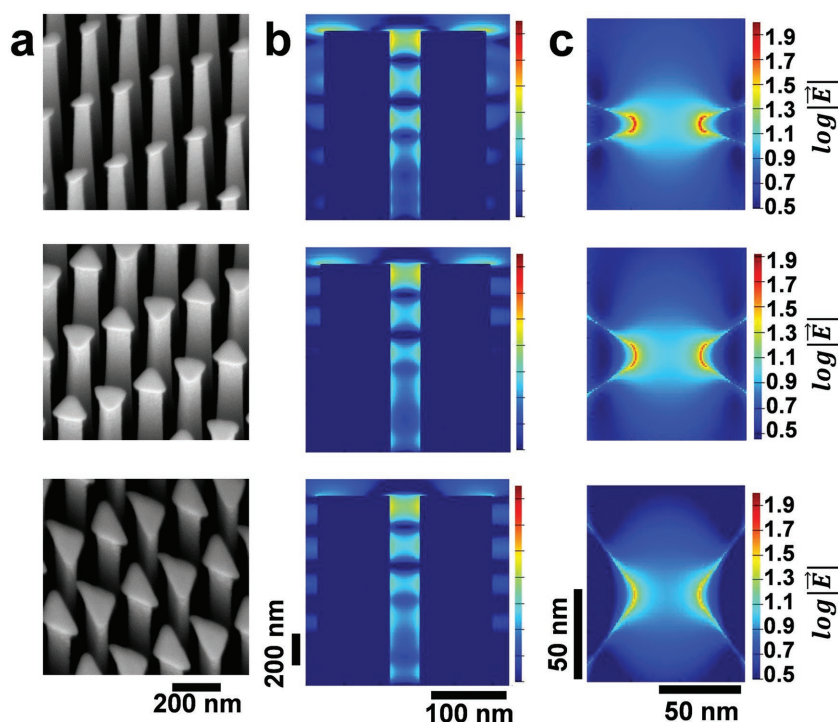


Figure 4. Calculated electric field amplitude distributions for 30° EBT, 60° EBT, and 100° EBT nanostructures. a) Top, middle, and bottom panels show SEM images of top of EBTs with $\Theta = 30^\circ$, 60° , and 100° apex angles, respectively. Images were taken at 30° from surface normal. b) Side view of electric field amplitude distributions on logarithmic jet color scale for three structures. Differences are observed in the gap region between the posts with 30° EBT showing highest enhancement close to the chromium bowtie. All three structures exhibit periodic fields in gap between posts. c) Zoomed view of gap region at chromium level observed from top shows strongest near-field enhancement at the apexes of 30° EBT, followed by 60° EBT and 100° EBT, respectively. A 337 nm wavelength p-polarized plane wave was injected from top of nanostructure at a 32° angle from surface normal and in plane with the bowtie axis.

internal energy, combined with the wider variety of fragment types, allows more in-depth structural characterization by LDI-MS from EBT than from NAPA.

To compare the sequence coverage for the two platforms in the case of a biologically relevant peptide, LDI spectra were collected for bradykinin. Here similar trends were observed to the case of P₁₄R, i.e., the fluence thresholds for the production of the protonated molecule were $\approx 4 \text{ mJ cm}^{-2}$ for EBT and $\approx 8 \text{ mJ cm}^{-2}$ for NAPA. At $\approx 40 \text{ mJ cm}^{-2}$, extensive fragmentation was observed in both cases; however, LDI from EBT revealed more γ -, b -, and a -series ions (Figure S5, Supporting Information). These findings demonstrate that information can be obtained on the primary structure of moderately sized peptides on both platforms, with enhanced sequence coverage for the EBT system.

6. Monitoring Chemical Reactions

Monitoring of enzyme-catalyzed reactions for biological macromolecules has been successfully demonstrated using other MS techniques, including electrospray ionization and MALDI.^[34] However, to minimize the ion suppression and matrix effects interfering with

the quantitation of enzymatic fragments using MALDI-MS, internal standards are necessary. Matrix-free LDI-MS techniques show promise to circumvent these challenges and provide time-resolved concentration profiles during enzymatic reactions.^[35] Trypsin, a common protease in bottom-up proteomics, has been used as a model for the kinetics of enzymatic degradation.^[34c,36] To determine the feasibility of using NAPA for quantitation of enzymatic reactions, we investigated the proteolytic digestion of the neuropeptide neurotensin (pGlu-LYENKPRRPYIL) resulting in the formation of RPYIL (fragment [9–13]) and pGlu-LYENKPR (fragment [1–8]). The tryptic reaction was monitored on a microscale for 60 min by taking 1 μL samples from a 300 μL mixture of the neuropeptide and the enzyme solutions. The samples were deposited on deep UV-projection lithography (DUV-PL) produced NAPA chips and dried before LDI-MS. Integrated signal from the LDI-MS (Figure 6a) of the chips for the digestion products and the undigested peptide were plotted as a function of the digestion time (Figure 6b–d). From the three response curves, the presence first-order kinetics was established. The rate coefficients for the production of the fragments at pH = 7.7 were $k_{m/z661} = 0.77 \pm 0.09 \times 10^{-3} \text{ s}^{-1}$ ($R^2 = 0.89$) and $k_{m/z1030} = 1.07 \pm 0.09 \times 10^{-3} \text{ s}^{-1}$ ($R^2 = 0.96$) and for the decomposition of the peptide was $k_{m/z1672} = 0.35 \pm 0.06 \times 10^{-3} \text{ s}^{-1}$ ($R^2 = 0.78$). The experimental design demonstrated here for the determination of rate coefficients can be applied for significantly more complex enzymatic digestion, degradation, and synthesis processes.

7. Trace Analysis of Cell Extracts and Tissue Sections on EBT Platforms

To demonstrate the feasibility of detecting components from trace amounts of biological samples, human hepatocellular carcinoma extracts, and mouse brain tissue sections were directly analyzed from the 60° EBT substrate. A small population (≈ 5000 cells) of HepG2/C3A cells was extracted by a polar solvent. The average volume of a human hepatocyte is $< 1 \text{ pL}$, thus the total volume of the analyzed cells was $< 5 \text{ nL}$. The extract was directly deposited onto the EBT structure, and in the mass spectrometer irradiated by laser pulses of 20 mJ cm^{-2} fluence. On average ≈ 373 sample-related peaks were observed (Figure 7a). Of the 20 common amino acids, 14 were detected (Ala, Gly, Pro, Glu, Cys, Ser, Leu, Asp, Gln, His, Arg, Phe, Tyr, and Trp) directly from this volume-limited complex sample. Being able to have a broad coverage of amino acids in a volume limited complex sample shows the utility of this high throughput method. A variety of other metabolites and lipids were also detected, including creatine, taurine, glycerylphosphorylethanolamine, palmitic acid (see Table S1 in the Supporting Information for annotations). Putative

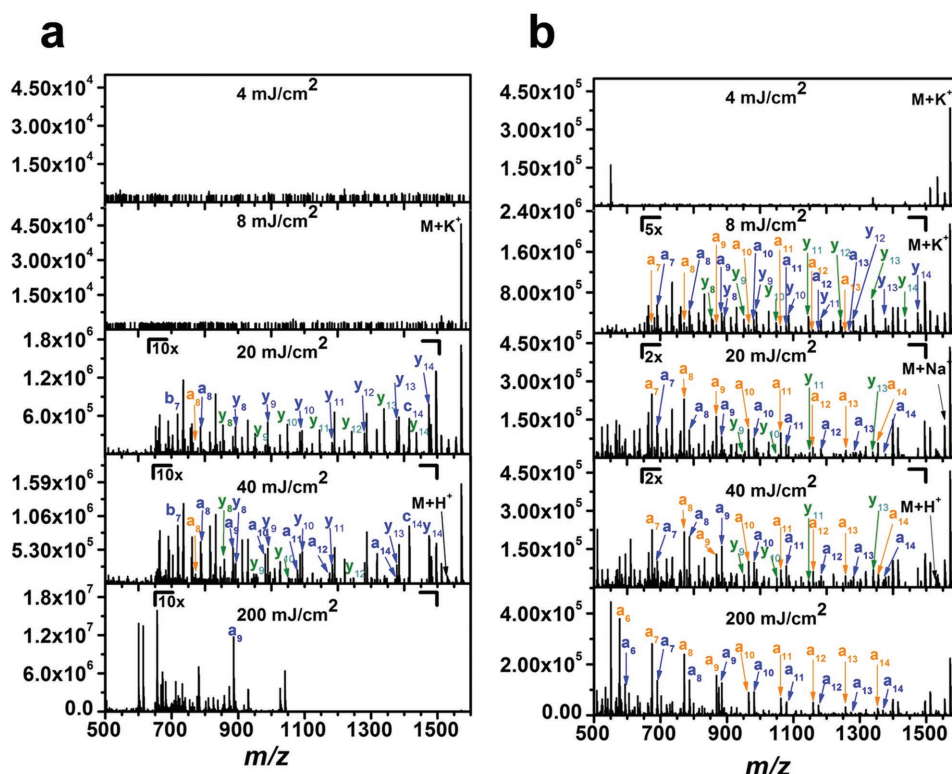


Figure 5. Comparison of fragmentation pattern induced by LDI of P₁₄R from a) NAPA and b) 60° EBT as a function of laser fluence. At 4 mJ cm⁻² spectra from EBT show quasimolecular ions, whereas there is no ion production from NAPA. Overall, EBT operates in a wider fluence range and produces more structure specific fragments.

annotations were based on accurate masses and on the spectra in our in-house small molecule library for 374 common metabolite standards that have been analyzed on NAPA.^[28a] Several ion

adducts were observed and were consistent with the metabolite standards analyzed by NAPA, including [M+K]⁺, [M+Na]⁺, [M+H-H₂O]⁺, [M+2Na-H]⁺, [M+2K-H]⁺, and [M+Na+K+H]⁺.

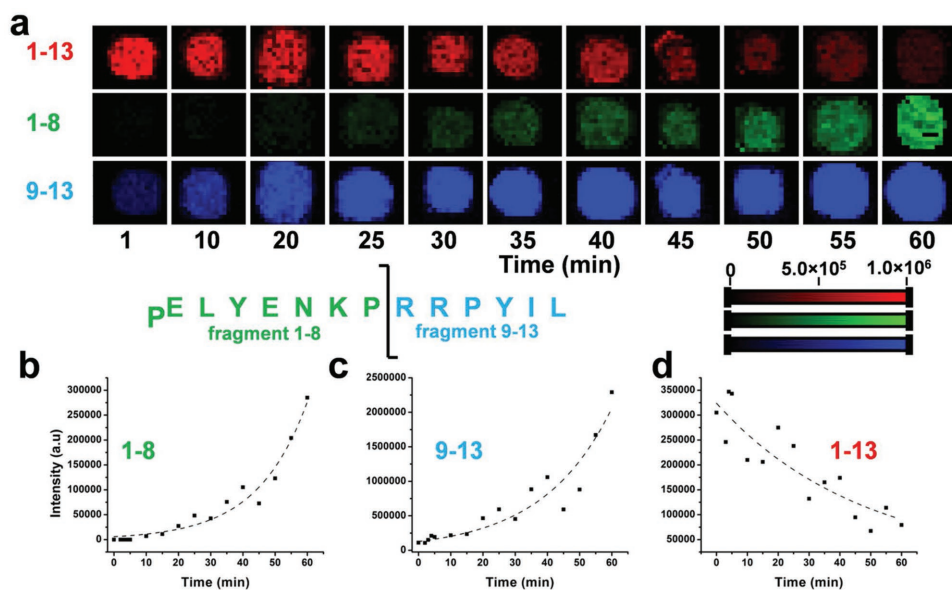


Figure 6. Tryptic digestion of neurotensin over a 60 min period followed by LDI-MS imaging on NAPA. a) Neurotensin intensity distributions are in top row (red), whereas those of tryptic fragments of [1–8] and [9–13] are in middle (green) and bottom (blue) rows, respectively. Signal intensities follow first order kinetics for b) precursor ($k_{m/z\ 1672} = 0.35 \pm 0.06 \times 10^{-3} \text{ s}^{-1}$; $R^2 = 0.78$) and c,d) product ions ($k_{m/z\ 661} = 0.77 \pm 0.09 \times 10^{-3} \text{ s}^{-1}$; $R^2 = 0.89$) and $k_{m/z\ 1030} = 1.07 \pm 0.09 \times 10^{-3} \text{ s}^{-1}$; $R^2 = 0.96$) as a function of digestion time.

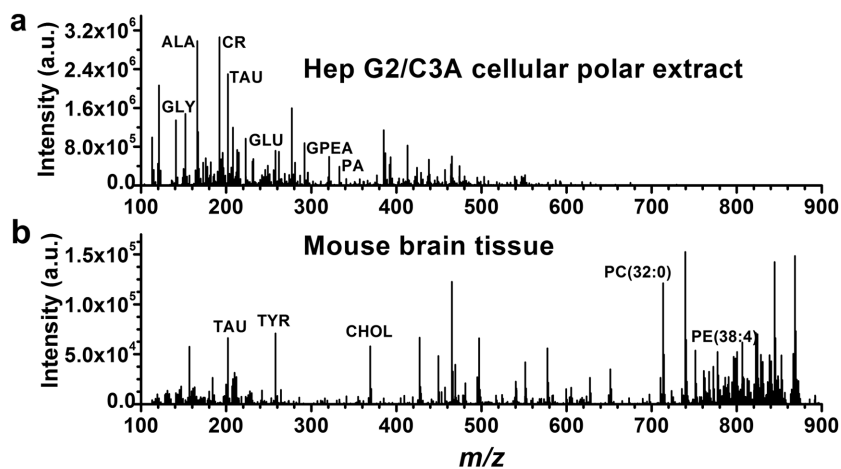


Figure 7. Complex biological samples analyzed by LDI-MS in positive ion mode directly from EBT nanostructures. a) Mass spectrum of a polar extract from ≈ 5000 HepG2/C3A cells revealed several metabolites, e.g., glycine (GLY), alanine (ALA), creatine (CR), taurine (TAU), glutamic acid (GLU), glycerylphosphorylethanolamine (GPEA), and palmitic acid (PA). b) Mass spectrum from the caudoputamen region of a $10\ \mu\text{m}$ thick mouse brain section. Small metabolites, e.g., taurine (TAU), tyrosine (TYR), and lipids, e.g., cholesterol (CHOL), phosphatidic acid (PA), and phosphatidylethanolamine (PE), were observed.

Tissue analysis was performed by thaw-mounting a $10\ \mu\text{m}$ thin coronal section of mouse brain directly onto the EBT substrate. To obtain the mass spectra, this sample was irradiated by a laser fluence of $100\ \text{mJ cm}^{-2}$, a five times higher value compared to the one used for the cell extracts. This difference can be attributed to the attenuation of the laser beam reaching the EBT substrate by the overlaid tissue section. The observed ≈ 337 spectral features included small molecules, i.e., amino acids and lipid species with very limited presence of interfering background peaks (see Figure 7b). Lipids can have diverse biological functions ranging from signaling to storage roles within cells. Due to this diversity, lipids present with varied chemical structures. The direct analysis and lipid profiling by LDI from EBT nanosubstrates of tissue sections provides insight into the composition of lipids without any manipulation to the sample surface. Of the observed spectral features, ≈ 170 were annotated to be lipid species, with detection of phosphatidylcholines, phosphatidylethanolamine, phosphatidylinositol, ceramides, and several lyso-lipid species (See Table S2 in the Supporting Information for annotations). Putative annotations were based on accurate mass measurements and previous MS imaging of mouse brain sections by LDI from NAPA substrates.^[28b]

8. Conclusions

Nanophotonic ionization by EBT relies on the interaction of these nanostructures with laser pulses. Compared to earlier NAPA-based systems, EBT exhibits several enhancements due to the interaction of the chromium bowties with the surface-parallel component of the oscillating electric field. These include lower fluence threshold for ionization, higher ion yields, and more efficient control over in-source fragmentation. Modeling of the electric field distributions indicated that the EBTs act more like an optical antenna array, whereas field enhancements

in NAPA structures were better described as the behavior of individual posts.

Matrix-free MS techniques provide unique opportunities for the analysis of small molecules by minimizing ion suppression and matrix effects present in conventional MALDI-MS. Applications of EBT as LDI substrates for MS showed excellent sensitivities and expanded ranges of quantitation compared to MALDI. Solution samples were analyzed for the monitoring of trypsin-catalyzed peptide digestion and tissue sections were tested for the potential of MS imaging. The extended dynamic range of analysis on EBT raises the possibility of quantitative MS imaging on these platforms. This would be a major step forward for imaging MS that currently relies mostly on MALDI and only offers semiquantitative performance. Further work includes exploring the utility of EBT substrates for quantitative MS imaging of biological tissue sections, and the effect of polarized laser radiation on ion production from EBT substrates.

9. Experimental Section

Elevated Bowtie and NAPA Nanofabrication: A $300\ \text{nm}$ thick layer ZEP520A positive e-beam resist was spin-coated directly on $4''$ low resistivity ($0.001\text{--}0.005\ \Omega\ \text{cm}$) p-type silicon wafers at $6000\ \text{rpm}$ for $45\ \text{s}$, and baked at $180\ ^\circ\text{C}$ for $2\ \text{min}$ to harden the resist. Through electron-beam lithography (JEOL JBX-9300, JEOL Ltd., Tokyo, Japan) the resist was patterned with bowtie arrays using an acceleration voltage of $100\ \text{kV}$ and exposure dose ranging between 300 to $525\ \mu\text{C cm}^{-2}$. Each wafer contained four quadrants with 36 identical chips with areas of $500 \times 500\ \mu\text{m}^2$ each. The four quadrants differed in the bowtie geometries, i.e., the bowties possessed apex angles of 30° , 60° , and 100° , and the fourth quadrant had chips with isolated bowties of 60° apex angle. For all bowtie arrays except for the isolated case, the gap size, post height, CCD, and RRD were kept constant at 40 , 1200 , 337 , and $200\ \text{nm}$, respectively. Once patterned, the resist was developed in a bath of xylenes for $30\ \text{s}$, washed with isopropanol, and dried with a stream of high-purity nitrogen gas. To remove impurities and residual resist, the wafers were exposed to oxygen plasma for $6\ \text{s}$ at $100\ \text{W}$ (Plasmalab System 100, Oxford Instruments, Yatton, Bristol, UK). Electron beam evaporation (VE-240 Thermionics Laboratory, Hayward, CA) was used to deposit a $12\ \text{nm}$ chromium layer on the whole wafer at a rate of $0.1\ \text{nm s}^{-1}$, this produced a chromium layer to form the bowtie pairs. To remove the unexposed resist and excess chromium, the wafers were sonicated in an acetone bath for $5\ \text{min}$ and an isopropanol bath for $2\ \text{min}$. The wafer was then rinsed with water for $2\ \text{min}$ and dried by a stream of high-purity nitrogen. To produce EBT arrays with heights of $1200\ \text{nm}$, reactive ion etching (RIE) at an etch rate of $100\ \text{nm min}^{-1}$ for silicon was performed on the processed wafers using the following etching gases: SF_6 , C_4F_8 , and Ar at 25 , 60 , and $5\ \text{sccm}$, respectively. The chromium bowties remained on top of the posts because they were not etched under these conditions. To characterize the produced bowtie dimensions a scanning electron microscope was used (Merlin, Carl ZEISS Microscopy Ltd., Jena, Germany). Energy dispersive X-ray point analyses of the top caps and Si posts were performed to ascertain the presence of Cr on the top of the posts, in which the $\text{K}\alpha 1$ features were only observed at the caps (See Figure S4 in the Supporting Information). The wafers were diced into smaller sections, e.g., to contain six chips in a row for easy insertion into the mass spectrometer.

Nanofabrication of the NAPA structures used in the comparisons with EBT arrays was identical to the process described in detail in an earlier publication.^[24a] The NAPA arrays in the experiments on quantitation of enzymatic digestion products were produced using a previously established protocol based on deep UV projection lithography.^[10b]

Laser Desorption Ionization from Nanophotonic Substrates: Unless otherwise stated, in all solution-based experiments, 500 nL aliquots were dispensed onto the six nanophotonic substrates within the wafer sections, and dried in a vacuum chamber at 75 Torr. Then the nanophotonic chips were mounted onto a standard MALDI plate with double-sided carbon tape. A hybrid mass spectrometer consisting of a linear ion trap and an orbitrap (MALDI LTQ-Orbitrap XL, Thermo Fisher Scientific Inc., Bremen, Germany) with a laser ionization source ($\lambda = 337$ nm wavelength and 60 Hz repetition rate) was used for LDI-MS acquisition from both the EBT and NAPA substrates. The laser fluence range was adjusted between 4 and 200 mJ cm⁻² to achieve acceptable ion yields, and the orbitrap mass resolving power was set to 30 000 with the automatic gain control turned off. The laser beam spot size was $\approx 100 \times 80 \mu\text{m}^2$ that was much larger in size than the CCD \times RRD of the nanostructures.

Mouse Brain Tissue and Cell Extract Analysis: Human hepatocellular carcinoma (HepG2/C3A; ATCC CRL-10741) cells were grown to confluence in 6 cm culture dishes at 37 °C in 5% CO₂ using Eagle's Minimum Essential Medium (ATCC 30-2003). The growth medium was pipetted off and the cells were rapidly washed with two 1 mL aliquots of 4 °C LC-MS grade water. The cells were then quenched with 1 mL of 70:30 methanol:water and incubated on dry ice for 5 min. After incubation, the cells were scraped from the dish and with the quench solution transferred to 2 mL microcentrifuge tubes, placed on ice, and homogenized with an ultrasonic probe (QSonica Q125, Newton, CT, USA; 30% intensity, 15 pulses, 1 s per pulse, 2 s between pulses). To remove the lipids, 1 mL of chloroform was added to each tube and the tubes were vortexed for 1 min, then incubated for 30 min at -20 °C. The samples were centrifuged at 14 000 \times g and 4 °C for 15 min, and the phases were isolated by pipetting. The aqueous layer was dried in a vacuum centrifuge and stored at -80 °C until use.

For tissue analysis six month old nude mice (J:NU) were obtained from Jackson Laboratories (Bar Harbor, ME, USA) and handled in accordance with the approved institutional animal use and care protocol (CNMC protocol # 30425). The healthy mice were euthanized by CO₂ asphyxiation, and the whole brain was extracted. Using a cryostat microtome (CM1800, Lecia Microsystems Inc., Nussloch, Germany), 10 μm thick coronal brain sections located within the 0.2–0.9 mm anterior from bregma were obtained. Due to the relatively small size of the available EBT chips, fragments of the coronal sections, e.g., from the caudoputamen, were directly thaw-mounted onto the chip. The chips with affixed tissue sections were immediately placed in a vacuum chamber with a pressure of 75 Torr for 5 min. Once the tissue dried, the chip was directly mounted by double sided carbon tape onto the standard MALDI plate for LDI-MS.

Proteolytic Digestion: Analysis of proteolytic mixtures was performed on NAPA chips that were fabricated by DUV-PL followed by RIE through a process described elsewhere in detail.^[10b] For the enzymatic digestion of neurotensin, a 13-residue neuropeptide, 200 μL of 0.3×10^{-3} M peptide solution was combined with 100 μL of 50×10^{-3} M ammonium bicarbonate buffer. To denature the peptide, the solution was heated to 95 °C for 5 min. For digestion, this solution was mixed with 1 μL of Gibco (0.25%) trypsin-EDTA and the mixture was maintained at 37 °C. To follow the digestion kinetics, 1 μL aliquots were taken at regular intervals for up to 60 min and deposited onto the 2 mm diameter DUV-PL NAPA chips. Each chip containing the lysates was then imaged using a step size of 100 μm resulting in ≈ 300 spectra from each chip that were averaged.

The intensities of the precursor peak, corresponding to residues 1–13, and the fragment peaks, corresponding to residues [1–8] and [9–13], were determined at each time point by performing MS imaging over the chips using a 100 μm step size. In ImageQuest, the ion intensities of the intact peptide and its fragments were averaged over the areas of the individual NAPA chips for each digestion time.

FDTD Model Simulations: In order to assess the field enhancement produced by the interaction of the laser light with the nanostructures, 3D FDTD calculations were conducted. To solve the time-dependent Maxwell's equations, the FDTD Solutions software package (Lumerical, Vancouver, BC, Canada) was used on a unit cell of the periodic nanostructure interacting with a nitrogen laser. Boundary conditions for the electric field distributions were set as antisymmetric and symmetric at the x - and y -minima, respectively, and perfectly matched layers (PML) were applied at the x - and y -maxima for the modeled domain. To represent the laser radiation consistent with the experiments, a p -polarized plane wave was injected from the top of the nanostructure at a 32° angle from surface normal and in plane with the bowtie axis. A variety of nanostructures were modeled, including EBT with varied bowtie antenna length, L , gap size, G , apex angle, $\Theta = 30^\circ, 60^\circ$, and 100° , apex radius of curvature, R , and bowtie elevation height, H , (see Figure 1a,b), NAPA, and isolated EBT. A fine mesh size of 1 nm was used for the modeling. The optical properties of silicon and chromium at the laser wavelength ($\lambda = 337$ nm for the nitrogen laser) were selected within the software and were based on literature data.^[37]

For the EBT array, silicon posts with triangular cross-sections of 100 nm height and a bowtie elevation height of $H = 1200$ nm were placed onto a flat silicon substrate. On top of the silicon posts, a 12 nm layer of chromium formed the EBT and the gap size between the two triangular halves was 40 nm throughout all the simulations. To vary the EBT apex angles between $\Theta = 30^\circ, 60^\circ$, and 100° , the heights of the triangular halves were kept constant at 100 nm, and the base lengths were set to 54, 115, and 238 nm, respectively.

For the NAPA and isolated EBT configurations, silicon posts with cylindrical and triangular cross-sections were constructed with diameters of 150 nm and base heights of 100 nm, respectively. Bowtie elevation and NAPA heights of $H = 1200$ nm were selected with a 12 nm layer of chromium on top in both cases. The periodicity in both cases followed the experimentally produced nanostructures, including the CCD = RRD = 337 nm, and the unit cells included pairs of posts.

Supporting Information

Supporting Information is available from the Wiley Online Library or from the author.

Acknowledgements

A.V., L.R.C., and S.A.S conceived the study, and S.A.S, L.R.C, A.R.K., and S.T.R. performed the nanofabrication of the EBT and NAPA substrates. S.A.S. and X.A.H., conducted the experiments. S.A.S. and A.V. performed the data analysis and the computational modeling, and S.A.S, A.R.K., and A.V. wrote the manuscript. Research was sponsored by the U.S. Army Research Office and the Defense Advanced Research Projects Agency and was accomplished under Cooperative Agreement Number W911NF-14-2-0020. The views and conclusions contained in this document are those of the authors and should not be interpreted as representing the official policies, either expressed or implied, of the Army Research Office, DARPA, or the U.S. Government. Application of the developed methods to mass spectrometry imaging was supported by the Division of Chemical Sciences, Geosciences, and Biosciences, Office of Basic Energy Sciences of the U.S. Department of Energy through Grant DE-FG02-01ER15129. S.A.S. is grateful for the scholarship award from the Achievement Rewards for College Scientists Foundation, Inc. (ARCS). The NAPA and EBT structures were nanofabricated, and a portion of the mass spectrometry data was obtained in the framework of a User Agreement (CNMS2013-309) at Oak Ridge National Laboratory's Center for Nanophase Materials Sciences, sponsored by the Scientific User Facilities Division, Office of Basic Energy Sciences, U.S. Department of Energy. The authors thank Dr. Christina Brantner for her help with the EDX measurements and SEM imaging and the Nanofabrication and Imaging Center of the The George Washington University for instrument access.

Conflict of Interest

The authors declare no conflict of interest.

Keywords

bowtie arrays, laser desorption, mass spectrometry, nanophotonic ionization, nanopost arrays

Received: March 9, 2018

Revised: April 18, 2018

Published online: May 22, 2018

- [1] J. A. Stolee, B. N. Walker, Y. Chen, A. Vertes, in *International Symposium on High Power Laser Ablation 2010* (Ed: C. R. Phipps), Vol. 1278, Melville, New York **2010**, p. 98.
- [2] a) E. Betzig, J. K. Trautman, *Science* **1992**, *257*, 189; b) R. M. Stockle, Y. D. Suh, V. Deckert, R. Zenobi, *Chem. Phys. Lett.* **2000**, *318*, 131; c) S. Thomas, G. Wachter, C. Lemell, J. Burgdorfer, P. Hommelhoff, *New J. Phys.* **2015**, *17*, 063010.
- [3] H. F. Hamann, M. Kuno, A. Gallagher, D. J. Nesbitt, *J. Chem. Phys.* **2001**, *114*, 8596.
- [4] A. Kinkhabwala, Z. F. Yu, S. H. Fan, Y. Avlasevich, K. Mullen, W. E. Moerner, *Nat. Photonics* **2009**, *3*, 654.
- [5] a) E. Hao, G. C. Schatz, *J. Chem. Phys.* **2004**, *120*, 357; b) N. A. Hatab, C. H. Hsueh, A. L. Gaddis, S. T. Retterer, J. H. Li, G. Eres, Z. Y. Zhang, B. H. Gu, *Nano Lett.* **2010**, *10*, 4952.
- [6] L. Novotny, B. Hecht, *Principles of Nano-Optics*, Cambridge University Press, Cambridge **2006**.
- [7] D. S. Cornett, M. L. Reyzer, P. Chaurand, R. M. Caprioli, *Nat. Methods* **2007**, *4*, 828.
- [8] a) M. Bucknall, K. Y. C. Fung, M. W. Duncan, *J. Am. Soc. Mass Spectrom.* **2002**, *13*, 1015; b) M. W. Duncan, G. Matanovic, A. Cerpapalj, *Rapid Commun. Mass Spectrom.* **1993**, *7*, 1090; c) G. Schlosser, G. Pocsfalvi, E. Huszar, A. Malorni, F. Hudecz, *J. Mass Spectrom.* **2005**, *40*, 1590; d) E. Szajli, T. Feher, K. F. Medzirhadszky, *Mol. Cell. Proteomics* **2008**, *7*, 2410; e) R. Knochenmuss, F. Dubois, M. J. Dale, R. Zenobi, *Rapid Commun. Mass Spectrom.* **1996**, *10*, 871; f) R. Knochenmuss, R. Zenobi, *Chem. Rev.* **2003**, *103*, 441.
- [9] a) Z. Guo, A. A. Ganawi, Q. Liu, L. He, *Anal. Bioanal. Chem.* **2006**, *384*, 584; b) D. Mark, S. Haerberle, G. Roth, F. von Stetten, R. Zengerle, *Chem. Soc. Rev.* **2010**, *39*, 1153; c) Y. C. Ho, M. C. Tseng, Y. W. Lu, C. C. Lin, Y. J. Chen, M. R. Fuh, *Anal. Chim. Acta* **2011**, *697*, 1.
- [10] a) M. Rainer, M. N. Qureshi, G. K. Bonn, *Anal. Bioanal. Chem.* **2011**, *400*, 2281; b) N. J. Morris, H. Anderson, B. Thibeault, A. Vertes, M. J. Powell, T. T. Razunguzwa, *RSC Adv.* **2015**, *5*, 72051.
- [11] J. Sunner, E. Dratz, Y. C. Chen, *Anal. Chem.* **1995**, *67*, 4335.
- [12] a) N. Bergman, D. Shevchenko, J. Bergquist, *Anal. Bioanal. Chem.* **2014**, *406*, 49; b) J. Wang, Q. Liu, Y. Liang, G. B. Jiang, *Anal. Bioanal. Chem.* **2016**, *408*, 2861; c) J. Wu, X. Wei, J. R. Gan, L. Huang, T. Shen, J. T. Lou, B. H. Liu, J. X. J. Zhang, K. Qian, *Adv. Funct. Mater.* **2016**, *26*, 4016; d) L. Huang, J. J. Wan, X. Wei, Y. Liu, J. Y. Huang, X. M. Sun, R. Zhang, D. D. Gurav, V. Vedarethinam, Y. Li, R. P. Chen, K. Qian, *Nat. Commun.* **2017**, *8*, 220.
- [13] L. M. Wei, Y. Xue, X. W. Zhou, H. Jin, Q. Shi, H. J. Lu, P. Y. Yang, *Talanta* **2008**, *74*, 1363.
- [14] P. Y. Hua, M. Manikandan, H. N. Abdelhamid, H. F. Wu, *J. Mater. Chem. B* **2014**, *2*, 7334.
- [15] C. S. Pan, S. Y. Xu, L. G. Hu, X. Y. Su, J. J. Ou, H. F. Zou, Z. Guo, Y. Zhang, B. C. Guo, *J. Am. Soc. Mass Spectrom.* **2005**, *16*, 883.
- [16] I. A. Popovic, M. Nestic, M. Vranjes, Z. Saponjic, M. Petkovic, *Anal. Bioanal. Chem.* **2016**, *408*, 7481.
- [17] I. Ocoy, B. Gulbakan, M. I. Shukoor, X. L. Xiong, T. Chen, D. H. Powell, W. H. Tan, *ACS Nano* **2013**, *7*, 417.
- [18] R. Nayak, D. R. Knapp, *Anal. Chem.* **2010**, *82*, 7772.
- [19] C. L. de Laorden, A. Beloqui, L. Yate, J. Calvo, M. Puigivila, J. Llop, N. C. Reichardt, *Anal. Chem.* **2015**, *87*, 431.
- [20] Y. Coffinier, S. Szunerits, H. Drobecq, O. Melnyk, R. Boukherroub, *Nanoscale* **2012**, *4*, 231.
- [21] J. Wei, J. M. Buriak, G. Siuzdak, *Nature* **1999**, *399*, 243.
- [22] R. A. Picca, C. D. Calvano, M. J. Lo Faro, B. Fazio, S. Trusso, P. M. Ossi, F. Neri, C. D'Andrea, A. Irrera, N. Cioffi, *J. Mass Spectrom.* **2016**, *51*, 849.
- [23] T. R. Northen, O. Yanes, M. T. Northen, D. Marrinucci, W. Uritboonthai, J. Apon, S. L. Golledge, A. Nordstrom, G. Siuzdak, *Nature* **2007**, *449*, 1033.
- [24] a) B. N. Walker, J. A. Stolee, D. L. Pickel, S. T. Retterer, A. Vertes, *J. Phys. Chem. C* **2010**, *114*, 4835; b) B. N. Walker, J. A. Stolee, A. Vertes, *Anal. Chem.* **2012**, *84*, 7756.
- [25] J. C. Meng, G. Siuzdak, M. G. Finn, *Chem. Commun.* **2004**, 2108.
- [26] R. D. Lowe, E. J. Szili, P. Kirkbride, H. Thissen, G. Siuzdak, N. H. Voelcker, *Anal. Chem.* **2010**, *82*, 4201.
- [27] X. Wei, Z. H. Liu, X. L. Jin, L. Huang, D. D. Gurav, X. M. Sun, B. H. Liu, J. Ye, K. Qian, *Anal. Chim. Acta* **2017**, *950*, 147.
- [28] a) A. R. Korte, S. A. Stopka, N. Morris, T. Razunguzwa, A. Vertes, *Anal. Chem.* **2016**, *88*, 8989; b) S. A. Stopka, C. Rong, A. R. Korte, S. Yadavilli, J. Nazarian, T. T. Razunguzwa, N. J. Morris, A. Vertes, *Angew. Chem., Int. Ed.* **2016**, *55*, 4482.
- [29] L. Sainiemi, H. Keskinen, M. Aromaa, L. Luosujarvi, K. Grigoras, T. Kotiaho, J. M. Makela, S. Franssila, *Nanotechnology* **2007**, *18*, 505303.
- [30] a) S. Alimpiev, A. Grechnikov, J. Sunner, V. Karavanskii, Y. Simanovsky, S. Zhabin, S. Nikiforov, *J. Chem. Phys.* **2008**, *128*, 014711; b) Y. E. Silina, M. Koch, D. A. Volmer, *J. Mass Spectrom.* **2015**, *50*, 578; c) B. N. Walker, J. A. Stolee, D. L. Pickel, S. T. Retterer, A. Vertes, *Applied Phys. A: Mater. Sci. Process.* **2010**, *101*, 539.
- [31] K. Q. d. Costa, V. Dmitriev, *J. Microwaves, Optoelectron. Electromagn. Appl.* **2010**, *9*, 123.
- [32] D. C. Reiber, T. A. Grover, R. S. Brown, *Anal. Chem.* **1998**, *70*, 673.
- [33] a) Y. Chen, A. Vertes, *Anal. Chem.* **2006**, *78*, 5835; b) J. A. Stolee, Y. Chen, A. Vertes, *J. Phys. Chem. C* **2010**, *114*, 5574.
- [34] a) B. Bothner, R. Chavez, J. Wei, C. Strupp, Q. Phung, A. Schneemann, G. Siuzdak, *J. Biol. Chem.* **2000**, *275*, 13455; b) S. Cheng, Q. H. Wu, H. Xiao, H. Chen, *Anal. Chem.* **2017**, *89*, 2338; c) Y. B. Pan, K. Cheng, J. W. Mao, F. J. Liu, J. Liu, M. L. Ye, H. F. Zou, *Anal. Bioanal. Chem.* **2014**, *406*, 6247.
- [35] J. J. Thomas, Z. X. Shen, J. E. Crowell, M. G. Finn, G. Siuzdak, *Proc. Natl. Acad. Sci. USA* **2001**, *98*, 4932.
- [36] J. V. Olsen, S. E. Ong, M. Mann, *Mol. Cell. Proteomics* **2004**, *3*, 608.
- [37] E. D. Palik, *Handbook of Optical Constants of Solids*, Elsevier Science, Oxford **2012**.

ADVANCED FUNCTIONAL MATERIALS

Supporting Information

for *Adv. Funct. Mater.*, DOI: 10.1002/adfm.201801730

Trace Analysis and Reaction Monitoring by Nanophotonic
Ionization Mass Spectrometry from Elevated Bowtie
and Silicon Nanopost Arrays

Sylwia A. Stopka, Xavier A. Holmes, Andrew R. Korte, Laine
R. Compton, Scott T. Retterer, and Akos Vertes**

Supporting Information

Title: Trace Analysis and Reaction Monitoring by Nanophotonic Ionization Mass Spectrometry from Elevated Bowtie and Silicon Nanopost Arrays

Sylwia A. Stopka, Xavier A. Holmes, Andrew R. Korte, Laine R. Compton, Scott T. Retterer, and Akos Vertes**

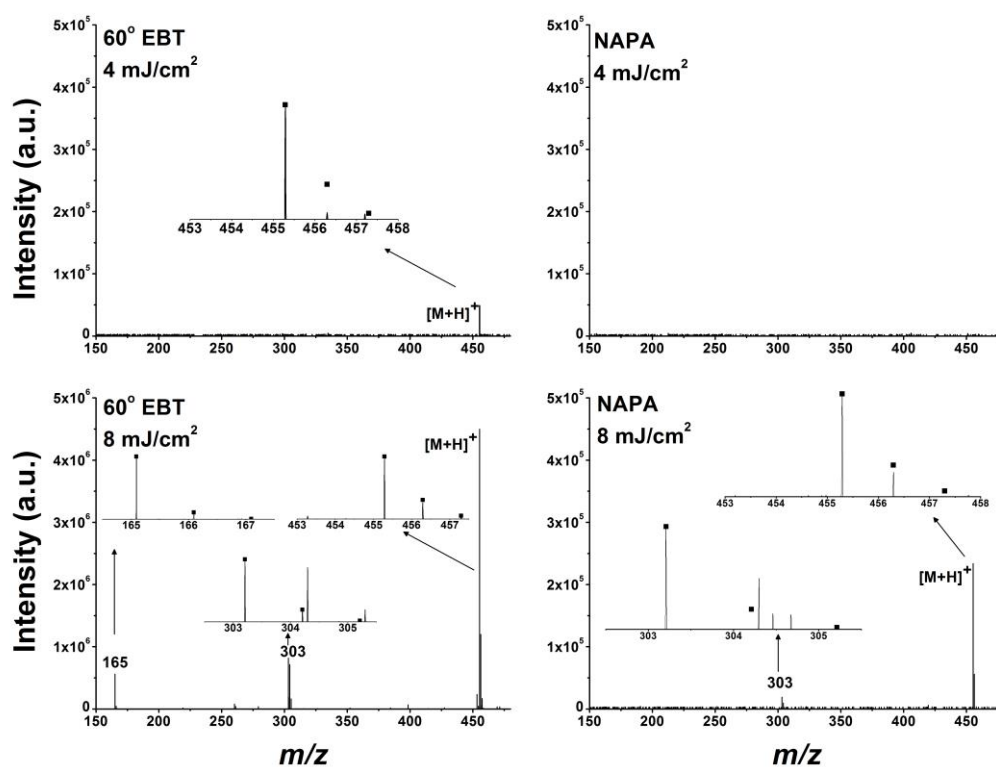


Figure S1. Verapamil mass spectra corresponding to Figure 2a for the 60° EBT and NAPA at 4 and 8 mJ/cm² laser fluences. Molecular ion peak was detected in the protonated form at m/z 455.2898, and two fragments were observed at m/z 303.2062 and m/z 165.0905 (see

insets for experimental isotopic patterns for these ions compared to the calculated centroid positions indicated by the black squares). The 60° EBT and NAPA nanostructures exhibited ionization thresholds of 4 mJ/cm² and 8 mJ/cm², respectively. Both structures induced higher fragmentation with increasing laser fluence. Additional fragmentation was observed on 60° EBT at 8 mJ/cm², where sample related fragments appeared at m/z 453.2745 and m/z 304.2992.

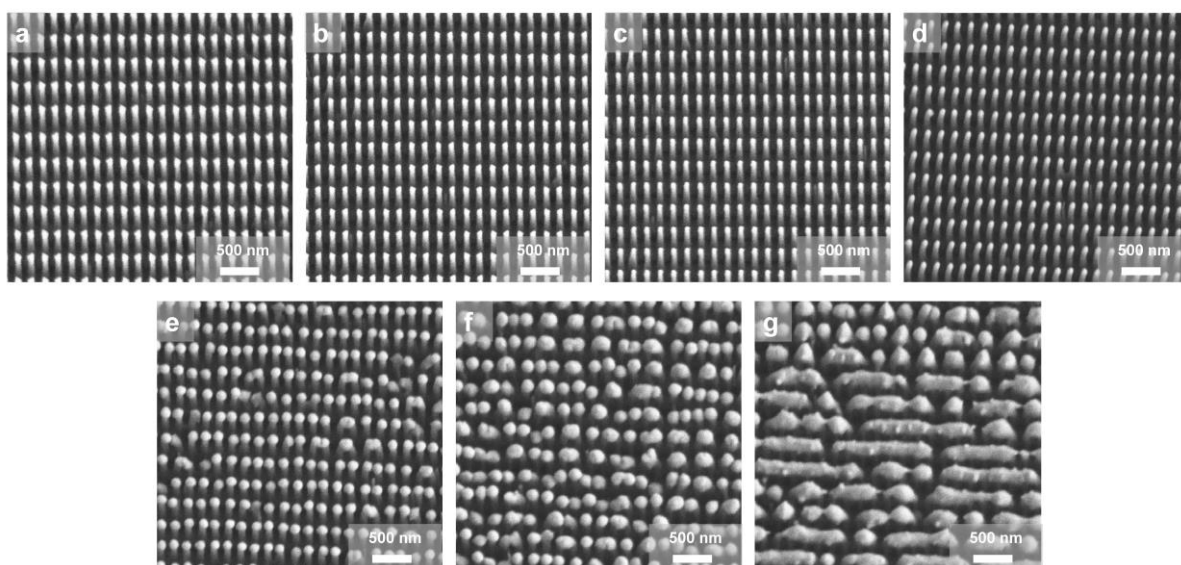


Figure S2. Morphologies of 60° EBT structures **a)** before and **b-g)** after laser exposure of 4, 8, 12, 16, 20, and 24 mJ/cm², respectively. At fluences up to 8 mJ/cm², no change in morphology is observed. At higher laser fluences, the chromium bowties are melted away and the silicon posts are increasingly deformed.

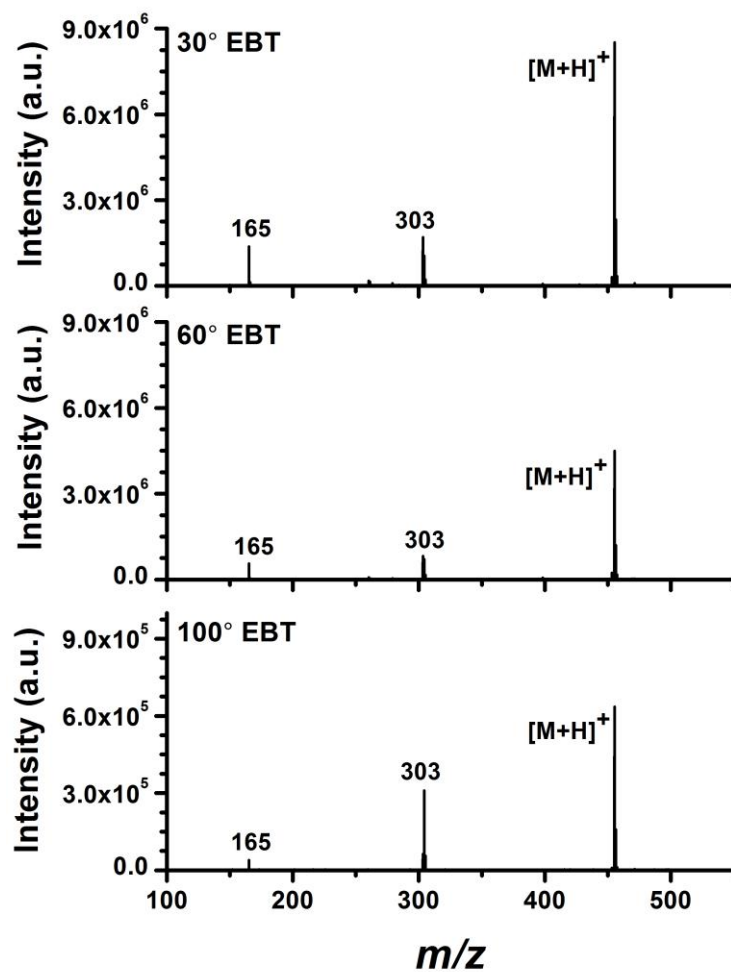


Figure S3. Verapamil mass spectra corresponding to 30° EBT, 60° EBT, and 100° EBT at a laser fluence of 8 mJ/cm^2 (spectra correspond to data in Figure 3a and 3b). Molecular ion was detected in the protonated form at m/z 455.2898 and two fragments were observed at m/z 303.2062 and m/z 165.0905.

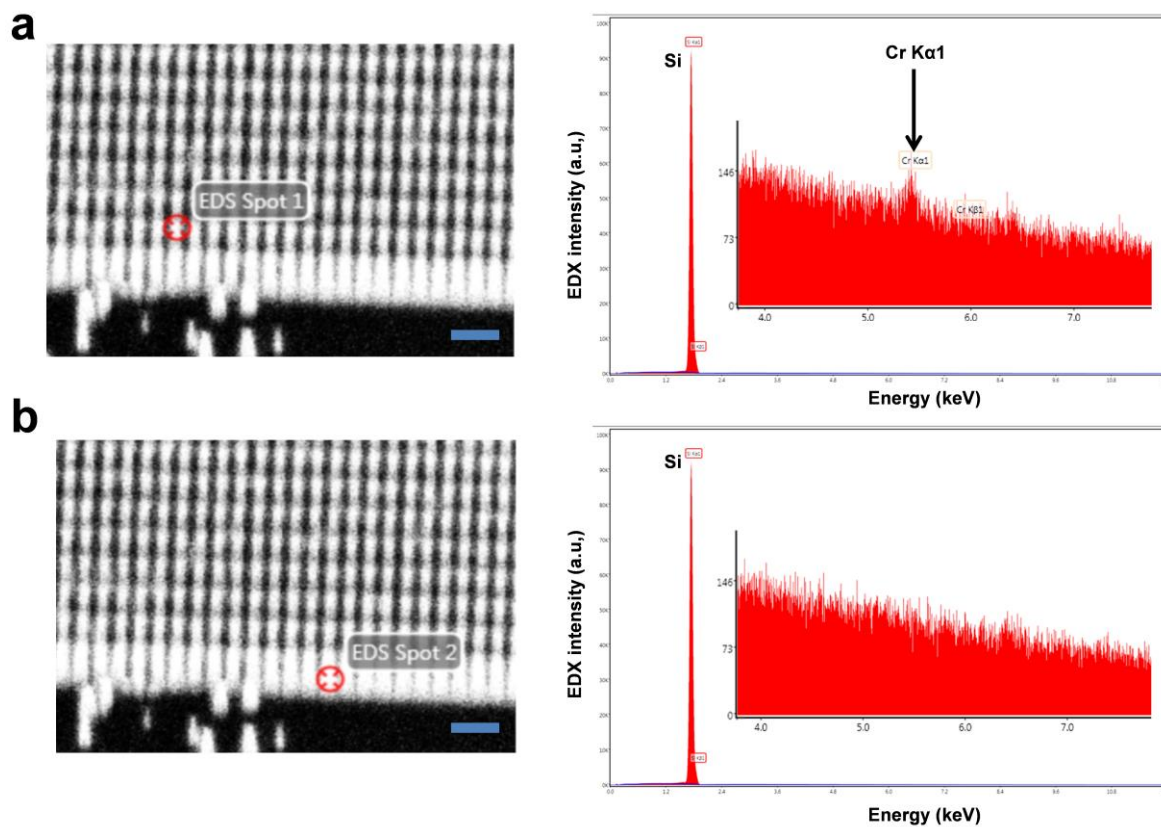


Figure S4. Local analysis of 60° EBT by energy dispersive X-ray detector (EDX) at **(a)** top of post revealing presence of Cr, and **(b)** at side of posts indicating that only silicon is present. Scale bars in images are 500 nm.

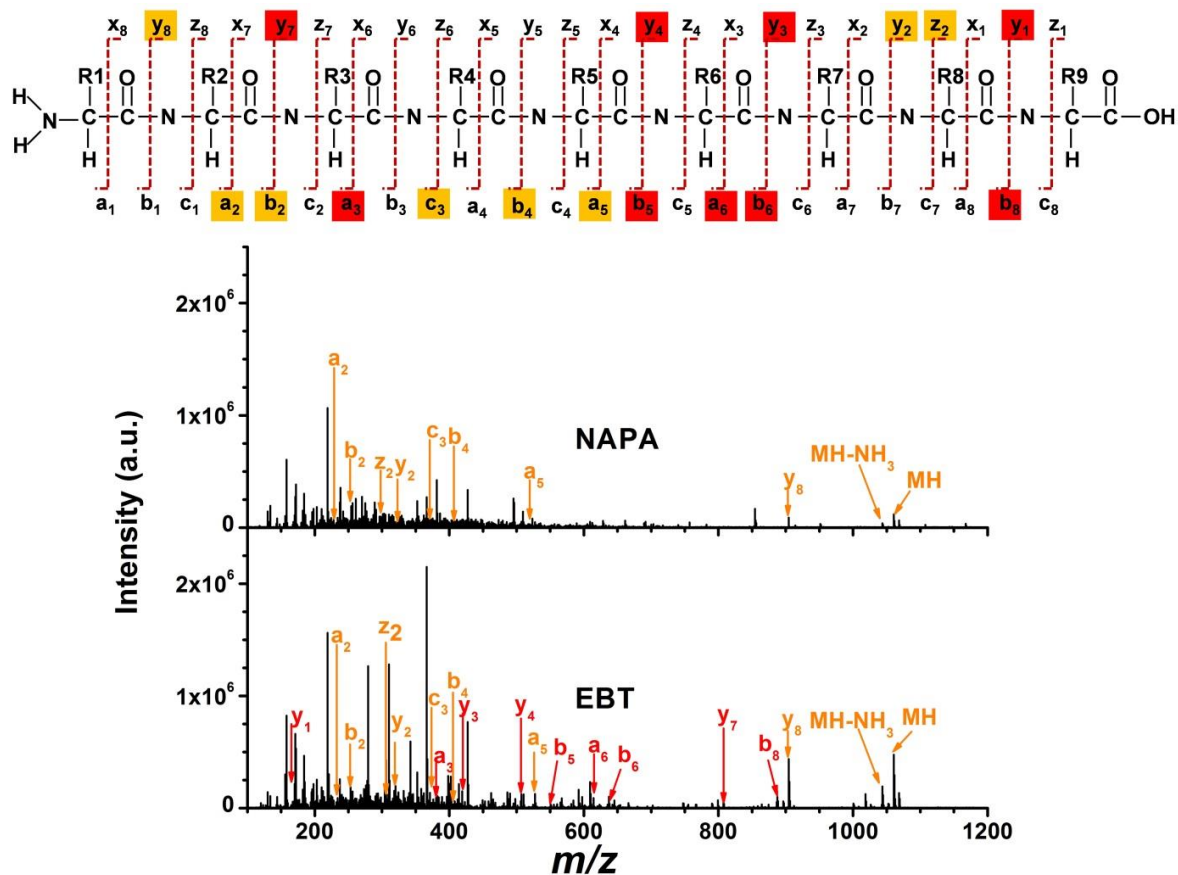


Figure S5. (Top panel) Enhanced sequence coverage for bradykinin by LDI from 60° EBT compared to NAPA. Cleavages present only in EBT spectra are marked red. (Bottom panel) Comparison of LDI mass spectra for bradykinin from NAPA and EBT at a laser fluence of ~ 40 mJ/cm² reveals more structure-specific N terminal (*a*, *b*, *c*) and C terminal (*y*, *z*) ions for the latter. Ions present only in EBT spectra are annotated in red.

Table S1. Putative annotation of positive ions from Hep G2/C3A cell extract

Annotation	Formula	Adduct	Meas. <i>m/z</i>	Calc. <i>m/z</i>	δ (mDa)
Glycine	C ₂ H ₅ NO ₂	[M+Na+K-H] ⁺	135.9772	135.9771	0.10
		[M+2K-H] ⁺	151.9451	151.9511	-6.00
Alanine	C ₃ H ₇ NO ₂	[M+Na+K-H] ⁺	149.9926	149.9928	-0.20
		[M+2K-H] ⁺	165.9660	165.9667	-0.70
Proline	C ₅ H ₉ NO ₂	[M+2Na-H] ⁺	160.0339	160.0345	-0.60
		[M+Na+K-H] ⁺	176.0077	176.0084	-0.70
Creatine	C ₄ H ₉ N ₃ O ₂	[M+K] ⁺	170.0325	170.0326	-0.10
		[M+2K-H] ⁺	207.9871	207.9885	-1.40
Glutamate	C ₅ H ₉ NO ₄	[M+2K-H] ⁺	223.9719	223.9722	-0.30

Threonine	C ₄ H ₉ NO ₃	[M+Na+K-H] ⁺	180.0032	180.0034	-0.20
		[M+2K-H] ⁺	195.9763	195.9773	-1.00
Cysteine	C ₆ H ₁₂ N ₂ O ₄ S ₂	[M+Na+K-H] ⁺	181.9607	181.9649	-4.20
Serine	C ₃ H ₇ NO ₃	[M+2K-H] ⁺	181.9607	181.9616	-0.90
Taurine	C ₂ H ₇ NO ₃ S	[M+Na+K-H] ⁺	185.9596	185.9598	-0.20
		[M+2K-H] ⁺	201.9258	201.9337	-7.90
Leucine	C ₆ H ₁₃ NO ₂	[M+Na+K-H] ⁺	192.0385	192.0397	-1.20
		[M+2K-H] ⁺	208.0131	208.0137	-0.60
Aspartate	C ₄ H ₇ NO ₄	[M+Na+K-H] ⁺	193.9796	193.9826	-3.00
Glutamine	C ₅ H ₁₀ N ₂ O ₃	[M+Na+K-H] ⁺	207.0136	207.0143	-0.70
		[M+2K-H] ⁺	222.9873	222.9882	-0.90
Histidine	C ₆ H ₉ N ₃ O ₂	[M+Na+K-H] ⁺	216.0141	216.0146	-0.50
		[M+2K-H] ⁺	231.9873	231.9885	-1.20
Phenylalanine	C ₉ H ₁₁ NO ₂	[M+Na+K-H] ⁺	226.0223	226.0241	-1.80
		[M+2K-H] ⁺	241.9966	241.9980	-1.40
Arginine	C ₆ H ₁₄ N ₄ O ₂	[M+Na+K-H] ⁺	235.0561	235.0568	-0.70
		[M+2K-H] ⁺	251.0294	251.0307	-1.30
Tyrosine	C ₉ H ₁₁ NO ₃	[M+Na+K-H] ⁺	242.0179	242.0190	-1.10
		[M+2K-H] ⁺	257.9920	257.9929	-0.90
Cystine	C ₆ H ₁₂ N ₂ O ₄ S ₂	[M+Na] ⁺	263.0183	263.0131	5.20
Tryptophan	C ₁₁ H ₁₂ N ₂ O ₂	[M+Na+K-H] ⁺	265.0331	265.0350	-1.90
		[M+2K-H] ⁺	281.0077	281.0089	-1.20
Cytidine	C ₉ H ₁₃ N ₃ O ₅	[M+2K-H] ⁺	320.0046	320.0046	0.00
Palmitic acid	C ₁₆ H ₃₂ O ₂	[M+2K-H] ⁺	333.1579	333.1593	-1.40

Table S2. Putative annotation of positive ions from mouse brain tissue section

Annotation	Formula	Adduct	Meas. <i>m/z</i>	Calc. <i>m/z</i>	δ (mDa)
Asparagine	C ₄ H ₈ N ₂ O ₃	[M+H-H ₂ O] ⁺	115.0549	115.0502	4.70
Glutamine	C ₅ H ₁₀ N ₂ O ₃	[M+H-H ₂ O] ⁺	129.0705	129.0659	4.60
Creatinine	C ₄ H ₇ N ₃ O	[M+K] ⁺	152.0235	152.0221	1.40
Creatine	C ₄ H ₉ N ₃ O ₂	[M+K] ⁺	170.0340	170.0326	1.40
Taurine	C ₂ H ₇ NO ₃ S	[M+Na+K-H] ⁺	185.9614	185.9598	1.60
		[M+2K-H] ⁺	201.9367	201.9337	3.00
Glutamine	C ₅ H ₁₀ N ₂ O ₃	[M+2K-H] ⁺	222.9898	222.9882	1.60
Glutamate	C ₅ H ₉ NO ₄	[M+2K-H] ⁺	223.9732	223.9722	1.00

Palmitic acid	$C_{16}H_{32}O_2$	$[M+2K-H]^+$	333.1616	333.1593	2.30
Cholesterol	$C_{27}H_{46}O$	$[M+H-H_2O]^+$	369.3522	369.3516	0.60
		$[M+Na]^+$	409.3440	409.3441	-0.10
		$[M+K]^+$	425.3177	425.3180	-0.30
PE (38:4)	$C_{43}H_{78}NO_8P$	$[M+K]^+$	806.5078	806.5097	-1.90
PC (32:0)	$C_{37}H_{71}O_8P$	$[M-N(CH_3)_3+K]^+$	713.4524	713.4518	0.60
PI-Cer (40:1)	$C_{46}H_{90}NO_{11}P$	$[M+H]^+$	864.634	864.6324	1.6
PA (38:2)	$C_{41}H_{77}O_8P$	$[M+K]^+$	767.4998	767.4988	1.0